Rebound suppression of a droplet impacting on an oscillating horizontal surface

K. Ashoke Raman,[1,*] Rajeev K. Jaiman,[1,†] Yi Sui,[2] Thong-See Lee,[1] and Hong-Tong Low[1]

[1]*Department of Mechanical Engineering, National University Singapore, 10 Kent Ridge Crescent, Singapore 117576, Singapore*
[2]*School of Engineering and Materials Science, Queen Mary University of London, London E1 4NS, United Kingdom*

The behavior of a droplet impinging onto a solid substrate can be influenced significantly by the horizontal motion of the substrate. The coupled interactions between the moving wall and the impacting droplet may result in various outcomes, which may be different from the usual normal droplet impact on a stationary wall. In this paper, we present a method to suppress drop rebound on hydrophobic surfaces via transverse wall oscillations, normal to the impact direction. The numerical investigation shows that the suppression of droplet rebound has a direct relationship with the oscillation phase, amplitude, and frequency. For a particular range of oscillation frequencies and amplitudes, a lateral shifting of the droplet position is observed along the oscillating direction. While large oscillation amplitude favors the process of droplet deposition, a high frequency promotes droplet rebound from the oscillating wall. A linear trend in the transition region between deposition and rebound is observed from a scaled phase diagram of the oscillation amplitude versus frequency. We provide a systematic investigation of drop deposition and elucidate the mechanism of rebound suppression through the temporal evolution of the nonaxial kinetic energy and the velocity flow field.

I. INTRODUCTION

The phenomenon of a droplet impacting on a solid surface is ubiquitous in nature and has been studied for decades both experimentally and numerically owing to its fundamental importance in several natural and industrial applications. Important dynamical aspects of the impact phenomenon were discussed in comprehensive reviews provided by Yarin [1] and Rein [2]. A droplet impacting on a solid surface may exhibit several physical outcomes, such as deposition, rebound, partial rebound, and splashing [3]. Droplet rebound is a desirable outcome in self-cleaning [4], antidew [5,6], and anticorrosion [7] applications where removal of droplets from the surface is required. However, it becomes indispensable to control drop rebound in areas pertaining to spray cooling [8], ink-jet printing [9], spray painting [10], and pesticide deposition [11]. In these applications, droplet rebound would lead to excess loss in the impacting fluid leading to increased costs. Moreover, droplet rebound in pesticide spraying on plant leaves would result in environmental pollution. Hence, there is a need to consider advanced methods which can lead to effective suppression of droplet rebound from the solid substrate.

The dynamical outcome of drop impact on the solid surface is a result of several factors, such as capillary and inertial forces, viscous resistance, wall wettability, and surface roughness. Droplet rebound is generally favored by high impact velocity, low viscosity, and high surface tension. A parametric study to investigate drop rebound was conducted by Rioboo *et al.* [3]. They found that an increase in the surface tension, impact velocity, and receding contact angle favors the process of droplet rebound. For aqueous solutions, the addition of flexible polymers was found to suppress droplet rebound [12]. In this case, the initial spreading phase was not altered, but the additives induced greater resistance during

the recoiling phase of the droplet due to the non-Newtonian viscous effects. The addition of surfactants [13] in droplet liquid leads to a decrease in surface energy, thereby changing the wetting properties. Reduction in the surface energy results in less vigorous recoiling and prevents drop rebound. Deng and Gomez [14] observed that ionic microdroplets impinging on conductive surfaces exhibited droplet deposition instead of bouncing off the surface. Mangili *et al.* [15] investigated the impact dynamics of a droplet onto a soft solid substrate. They reported that the droplet undergoes slower recoiling and has a larger final resting diameter as compared to its impact onto a hard substrate. Antonini *et al.* [16] conducted experiments of droplet impact onto surfaces with different advancing and receding contact angles and found out that the receding contact angle as one of the key wetting parameters contributing to the droplet rebound. The droplet rebound time had a decreasing trend as the receding contact angle increased. Such behavior was also observed by the lattice Boltzmann method (LBM) simulations performed by Raman *et al.* [17]. In addition to the role of the receding contact angle, the authors [17] also found that the presence of inhomogeneities in the wetting characteristics in the form of a wetting gradient would lead to suppression of the drop rebound. Recently, Unnikrishnan *et al.* [18] performed experiments of droplet impact onto three chemically modified aluminum substrates. The receding velocities of the droplet in its recoiling phase for the aluminum substrates coated with octadecyltrichlorosilane were three times as that of drops on the aluminum substrate.

The above mentioned methods to suppress drop rebound involve either modifying the chemical properties of the droplet liquid or altering the physiochemical properties of the solid surface. Such alterations may not be desirable for certain applications, and the need to explore alternate methods which do not resort to chemical modification of either droplet liquid or solid surface becomes imperative. Rebound suppression of impacting drops with electrically driven nonaxisymmetric shapes on hydrophobic surfaces were reported by Yun *et al.* [19]. Such impinging droplets undergo alternate spread-

*ashokeraman@gmail.com
†mperkj@nus.edu.sg

ing and recoiling on the surface, which leads to transfer of kinetic energy (KE) along the principal horizontal axis rather than the vertical axis. They found a considerable increase in the critical Weber number (We) giving rise to rebound than that for an axisymmetric drop. Lee and Kim [20] investigated the recoil behavior of a droplet impacting on a surface moving along the vertical direction. Their investigations revealed that droplet rebound is promoted when the surface moves upward at the moment of impact, whereas the drop rebound suppression was observed when the surface moved downward at the impact moment. They attributed this behavior to the change in the impact speed of the droplet due to the surface motion. In this paper, we present a method for drop rebound control via external surface oscillations perpendicular to the line of impact. Through a set of numerical simulations, we probe the effects of oscillation amplitude and frequency on the impact dynamics and the time-dependent outcome. The results are illustrated through the time resolved interface profiles, the time evolution of contact diameter, the shift in center of mass of the droplet system, and the aspect ratio (AR) of the contact area. We provide a phase diagram of oscillation amplitude and frequencies wherein droplet rebound and suppression are noticed. The mechanism of rebound suppression is explained through the temporal evolution of nonaxial kinetic energy of the droplet.

To investigate the dynamics of rebound suppression via wall oscillations, we employ the lattice Boltzmann method in the present study. Over the past two decades, the lattice Boltzmann method has evolved as a powerful tool to simulate interfacial dynamics and multiphase flows. In contrast to the numerical solvers based on finite volume, difference, and element methods to solve the continuum Navier-Stokes equations, the LBM [21,22] is a simplified mesoscopic reduced-order kinetic model based on the Boltzmann equation. It solves the evolution of a particle distribution function, and the macroscopic quantities are obtained from the hydrodynamic moments of these distribution functions. In comparison with a solution of the Navier-Stokes equations, the lattice Boltzmann equations (LBEs) offer a simple, efficient, and easily parallelizable system. With its basis in the kinetic gas theory, the mesoscopic features of the LBM have been

useful in simulating the interface boundary between two binary fluids. As such, the LBM has been successfully employed in solving many multiphase flow problems [22–24]. Some of the distinct multiphase LBM models include the color gradient model [25,26], the interparticle potential model [27], the free-energy model [28], and the index-function model [29]. The free-energy and the index-function models solve a separate equation for the evolution of the interface, unlike the color gradient and potential models. The liquid-gas density ratios achieved with the model proposed by He *et al.* [29] was small. Lee and Lin [30] enhanced the model of He *et al.* [29] to capture two-phase flows with high-density ratios with a three step discretized LBE system. The authors in Ref. [30] proposed a compact isotropic finite differencing scheme to discretize the gradients of intermolecular forcing terms which eliminates spurious currents successfully. The authors have employed the treatment given in Ref. [31] on the characteristics of stress and potential forms related to the pressure tensor.

The paper is organized as follows: Sec. II outlines the details of the problem definition. In Sec. III we discuss the numerical formulation followed by validation in Sec. IV. The results on the dynamics on drop impact on an oscillating surface are presented and discussed in Sec. V. The essential mechanism of rebound suppression is elucidated in Sec. VI. Concluding remarks are provided in Sec. VII.

II. PROBLEM STATEMENT

A sketch outlining the problem definition is provided in Fig. 1. The droplet and the surrounding fluid are considered to be incompressible, viscous, and immiscible, and the surface tension coefficient is assumed to be constant. The droplet density and viscosity are denoted by ρ_l and μ_l, respectively, whereas those of the surrounding fluid are represented by ρ_g and μ_g as shown in the figure.

A droplet of diameter D_o impinges normally onto a solid surface with an impact velocity of U_o. The solid surface oscillates horizontally with a wall velocity of U_w. All the length and velocity scales are made nondimensional by the initial droplet diameter (D_o) and the impact velocity (U_o), respectively. Accordingly, the nondimensional time is given
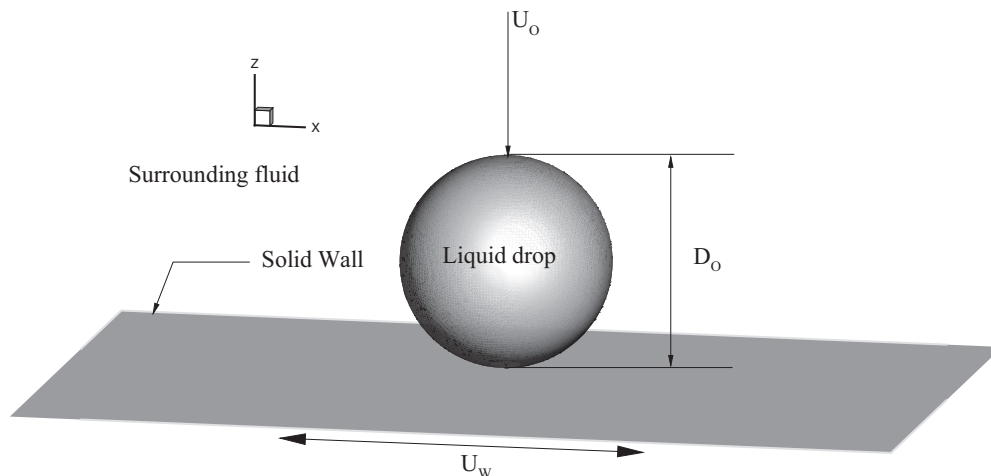
FIG. 1. Schematic of a liquid droplet impacting on a horizontally oscillating solid surface.

as $T^* = tU_o/D_o$, where t is the simulation time in lattice units. The important dimensionless parameters governing droplet impact on the solid substrate include the Weber number We $= \rho_l U_o^2 D_o/\sigma$, which indicates the ratio of inertial force to surface tension; the Reynolds number (Re) Re $= \rho_l U_o D_o/\mu_l$, which denotes the ratio of inertial force to viscous force; the Bond number (Bo) Bo $= (\rho_l - \rho_g)g D_o^2/\sigma$ measures the relative importance of surface tension force compared to gravity force, and the Ohnesorge number (Oh) Oh $= \mu_l/\sqrt{\rho D_i \sigma} = \sqrt{\text{We}}/\text{Re}$ relates the viscous forces to inertial and surface tension forces where σ is the liquid-gas surface tension. The density ratio $\rho_r = \rho_l/\rho_g$ and viscosity ratio $\mu_r = \mu_l/\mu_g$ in the current paper are set to be $\rho_r = 1000$ and $\mu_r = 40$, respectively. The realistic dimensions of the droplets considered in this study are in micrometers as illustrated in the validation section later. Hence, the effects of gravity are considered to be negligible whereby the radius of the droplet is smaller than the capillary length. The resulting Bond number for the impacting droplet would be of the order of $O(10^{-4})$. To investigate the role of surface oscillations, we set the Reynolds number and the Weber number of the impinging droplet at Re $= 600$ and We $= 51.2$, respectively. The computational domain is a cuboid with its nondimensional size set to be $4.0 \times 2.44 \times 1.72$. The no-slip wall boundary conditions are applied on the top and bottom boundaries. For the bottom boundary, the no-slip boundary condition is imposed using the bounce back scheme [32] in which the colliding particles not only reverse their momenta, but also gain

momentum due to the wall velocity U_w. Periodic boundary conditions are imposed on the side boundaries. The wall oscillates with an amplitude of U_A and frequency ω, which is given by

$$\omega = (\bar{\omega}\pi)/T_{\text{iner}}, \tag{1}$$

where T_{iner} is the inertial time scale defined as $T_{\text{iner}} = D_o/U_o$. In the subsequent sections, the wall oscillations will be characterized by a simple wave form as a function of oscillating velocity amplitude U_A and the frequency $\bar{\omega}$: $U_w = U_A f(\bar{\omega}, T^* + \psi)$, where the function f can take the form of sinusoidal and nonsinusoidal (square and triangle) waves with corresponding phase angle ψ.

III. MATHEMATICAL FORMULATION

In the present study, the dynamics of an impacting droplet on an oscillating surface is simulated by a high-density ratio multiphase lattice Boltzmann solver which has been discussed and validated in our previous publications [17,33]. This method [30] employs two particle distribution functions to recover the incompressible Navier-Stokes equation (g_α) and a macrointerface capturing equation (f_α.) The model adopts stress and potential forms of intermolecular forcing terms in the momentum equation and the equation for order parameter, respectively.

The distribution functions are solved in a three step process as follows: (i) *Prestreaming step*,

$$\bar{g}_\alpha(\mathbf{x},t) = g_\alpha(\mathbf{x},t) - \frac{g_\alpha - g_\alpha^{\text{eq}}}{2\tau}\bigg|_{(\mathbf{x},t)} + \frac{\delta t}{2}\frac{(e_{\alpha i} - u_i)\partial_i(\rho c_s^2)}{c_s^2}[\Gamma_\alpha(\mathbf{u}) - \Gamma_\alpha(0)]\bigg|_{(\mathbf{x},t)}$$
$$+ \frac{\delta t}{2}\frac{(e_{\alpha i} - u_i)[\kappa\partial_i(\partial_k\rho\partial_k\rho) - \kappa\partial_j(\partial_j\rho\partial_i\rho)]}{c_s^2}\Gamma_\alpha(\mathbf{u})\bigg|_{(\mathbf{x},t)}, \tag{2}$$

$$\bar{f}_\alpha(\mathbf{x},t) = f_\alpha(\mathbf{x},t) - \frac{f_\alpha - f_\alpha^{\text{eq}}}{2\tau}\bigg|_{(\mathbf{x},t)} + \frac{\delta t}{2}\frac{(e_{\alpha i} - u_i)[\partial_i\rho c_s^2 - \rho\partial_i(\phi - \kappa\partial_j^2\rho)]}{c_s^2}\Gamma_\alpha(\mathbf{u})\bigg|_{(\mathbf{x},t)}. \tag{3}$$

(ii) *Streaming*,

$$\bar{g}(\mathbf{x} + \mathbf{e}_\alpha\delta t, t + \delta t) = \bar{g}_\alpha(\mathbf{x},t), \tag{4}$$

$$\bar{f}(\mathbf{x} + \mathbf{e}_\alpha\delta t, t + \delta t) = \bar{f}_\alpha(\mathbf{x},t). \tag{5}$$

(iii) *Poststreaming step*,

$$g_\alpha(\mathbf{x} + \mathbf{e}_\alpha\delta t, t + \delta t) = \bar{g}_\alpha(\mathbf{x} + \mathbf{e}_\alpha\delta t, t + \delta t) - \frac{1}{2\tau + 1}(\bar{g}_\alpha - \bar{g}_\alpha^{\text{eq}})\bigg|_{(\mathbf{x} + \mathbf{e}_\alpha\delta t, t + \delta t)}$$
$$+ \frac{2\tau}{2\tau + 1}\frac{\delta t}{2}\frac{(e_{\alpha i} - u_i)\partial_i(\rho c_s^2)}{c_s^2}[\Gamma_\alpha(\mathbf{u}) - \Gamma_\alpha(0)]\bigg|_{(\mathbf{x} + \mathbf{e}_\alpha\delta t, t + \delta t)}$$
$$+ \frac{2\tau}{2\tau + 1}\frac{\delta t}{2}\frac{(e_{\alpha i} - u_i)[\kappa\partial_i(\partial_k\rho\partial_k\rho) - \kappa\partial_j(\partial_j\rho\partial_i\rho)]}{c_s^2}\Gamma_\alpha(\mathbf{u})\bigg|_{\mathbf{x} + \mathbf{e}_\alpha\delta t, t + \delta t}, \tag{6}$$

$$f_\alpha(\mathbf{x} + \mathbf{e}_\alpha\delta t, t + \delta t) = \bar{f}_\alpha(\mathbf{x} + \mathbf{e}_\alpha\delta t, t + \delta t)$$
$$- \frac{1}{2\tau + 1}(\bar{f}_\alpha - f_\alpha^{\text{eq}})\bigg|_{(\mathbf{x} + \mathbf{e}_\alpha\delta t, t + \delta t)}$$
$$+ \frac{2\tau}{2\tau + 1}\frac{\delta t}{2}\frac{(e_{\alpha i} - u_i)[\partial_i\rho c_s^2 - \rho\partial_i(\phi - \kappa\partial_j^2\rho)]}{c_s^2}\Gamma_\alpha(\mathbf{u})\bigg|_{(\mathbf{x} + \mathbf{e}_\alpha, t + \delta t)}. \tag{7}$$
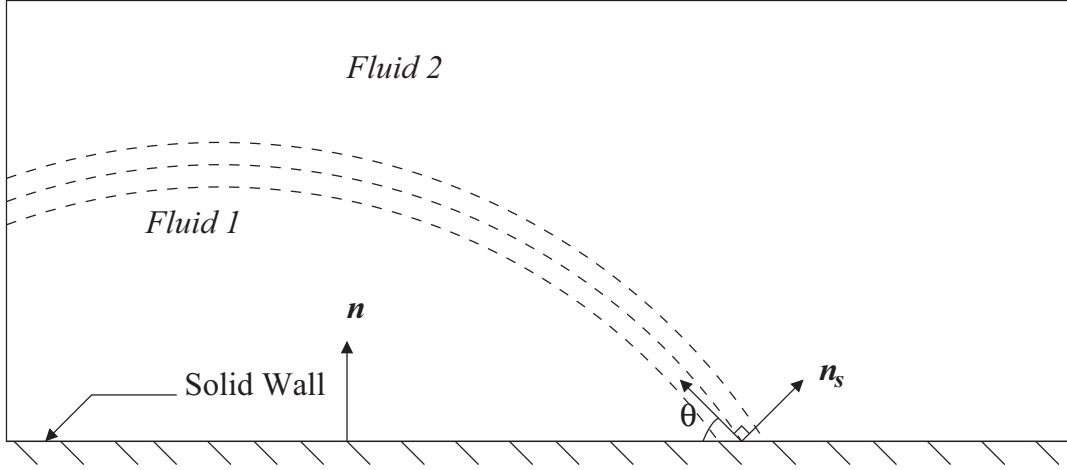
FIG. 2. Schematic of a liquid drop on a solid surface with a contact angle. The diffused interface is shown by dashed lines.

The equilibrium distribution functions are given by

$$f_\alpha^{\text{eq}} = w_\alpha \rho \left[1 + \frac{\mathbf{e}_\alpha \cdot \mathbf{u}}{c_s^2} + \frac{(\mathbf{e}_\alpha \cdot \mathbf{u})^2}{2c_s^4} - \frac{(\mathbf{u} \cdot \mathbf{u})}{2c_s^2} \right], \qquad (8)$$

$$g_\alpha^{\text{eq}} = w_\alpha \left[\frac{p}{c_s^2} + \frac{\rho \mathbf{e}_\alpha \cdot \mathbf{u}}{c_s^2} + \frac{\rho(\mathbf{e}_\alpha \cdot \mathbf{u})^2}{2c_s^4} - \frac{\rho(\mathbf{u} \cdot \mathbf{u})}{2c_s^2} \right], \quad (9)$$

where $c_s = 1/\sqrt{3}$ and w_α is the corresponding integral weights for a D3Q19 lattice velocity model,

$$\begin{aligned} w_\alpha &= \tfrac{1}{3}, && \alpha = 0, \\ w_\alpha &= \tfrac{1}{18}, && \alpha \in [1,6], \\ w_\alpha &= \tfrac{1}{36}, && \alpha \in [7,18], \end{aligned} \qquad (10)$$

and

$$\Gamma_\alpha(\mathbf{u}) = w_\alpha \left[1 + \frac{\mathbf{e}_\alpha \cdot \mathbf{u}}{c_s^2} + \frac{(\mathbf{e}_\alpha \cdot \mathbf{u})^2}{2c_s^4} - \frac{(\mathbf{u} \cdot \mathbf{u})}{2c_s^2} \right]. \qquad (11)$$

The chemical potential ϕ is given by

$$\phi \approx 4\beta (\rho - \rho_v^{\text{sat}})(\rho - \rho_l^{\text{sat}}) \left[\rho - \tfrac{1}{2}(\rho_v^{\text{sat}} + \rho_l^{\text{sat}}) \right], \qquad (12)$$

where β is a constant and ρ_v^{sat} and ρ_l^{sat} are the saturation densities of the vapor and liquid phases, respectively. The interface thickness, denoted as D, is given by

$$D = \frac{4}{(\rho_l^{\text{sat}} - \rho_v^{\text{sat}})} \sqrt{\frac{\kappa}{2\beta}}, \qquad (13)$$

where κ is a constant related to the magnitude of the surface tension. The surface tension force σ is represented as

$$\sigma = \frac{(\rho_l^{\text{sat}} - \rho_v^{\text{sat}})^3}{6} \sqrt{2\kappa\beta}. \qquad (14)$$

The density of the fluid ρ, hydrodynamics pressure p, and the velocity $\mathbf{u}$ are calculated by taking the moments of the corresponding distribution function,

$$\rho = \sum_\alpha \bar{f}_\alpha, \qquad (15)$$

$$p = \sum_\alpha \bar{g}_\alpha c_s^2 + \frac{\delta t}{2} u_i \frac{\partial \rho c_s^2}{\partial x_i}, \qquad (16)$$

$$u_i = \sum_\alpha g_\alpha \mathbf{e}_\alpha + \frac{\delta t}{2} \kappa \left[\frac{\partial}{\partial x_i} \left(\frac{\partial \rho}{\partial x_k} \frac{\partial \rho}{\partial x_k} \right) - \frac{\partial}{\partial x_j} \left(\frac{\partial \rho}{\partial x_i} \frac{\partial \rho}{\partial x_j} \right) \right]. \qquad (17)$$

The relaxation parameter τ is related to the kinematic viscosity $\nu = \tau c_s^2 \delta t$, which can be calculated by a linear interpolation,

$$\tau = C\tau_l - (1 - C)\tau_v, \qquad (18)$$

where τ_l and τ_v are the relaxation times for liquid and vapor, respectively, and C is the composition approximated by

$$C = \frac{(\rho - \rho_v^{\text{sat}})}{(\rho_l^{\text{sat}} - \rho_l^{\text{sat}})}. \qquad (19)$$

Along with the consistent discretizations of the intermolecular forcing terms, the aforementioned two-phase LBE formulation provides necessary stabilization at high-density and viscosity ratios. Although the mixed difference scheme is used in the pre-streaming collision step, the second-order central difference scheme is considered for the forcing terms in the poststreaming collision step. Further details on the discretization schemes can be found in Ref. [30].

For the wetting boundary condition, we employ a geometric formulation proposed by Ding and Spelt [34]. This geometric scheme has also been employed in the framework of the LBM to investigate the dynamics of sliding droplets on ideal and nonideal surfaces [35]. It assumes the density contours in the interface to be parallel to each other including the regions near the solid surface. This assumption relies on the fact that the interface is in the equilibrium or near equilibrium conditions at the solid surface. As such it is not applicable for scenarios where the interface near the contact region may significantly be thinned or thickened during computations. Furthermore, the interface has to be resolved by four to eight grid points. For a diffuse interface method, it is required that the interface and the region near the contact line have enough grid points to capture the droplet dynamics.

Figure 2 shows a schematic of the interface near the three phase contact region. The unit vector $\boldsymbol{n}_s$, perpendicular to the interface near the surface, is given by the following geometric

relationship:

$$\boldsymbol{n}_s = \frac{\nabla \rho}{|\nabla \rho|}. \tag{20}$$

The gradient of the scalar field ρ can be decomposed into the tangential and normal components along the two-dimensional plane as

$$\nabla \rho = (\boldsymbol{n} \cdot \nabla \rho)\boldsymbol{n} + (\boldsymbol{t} \cdot \nabla \rho)\boldsymbol{t}, \tag{21}$$

where $\boldsymbol{t}$ and $\boldsymbol{n}$ are the unit tangential and normal vectors on the surface, respectively. Hence from Fig. 2, the three-phase contact angle θ can be computed geometrically in terms of density ρ by

$$\tan\left(\frac{\pi}{2} - \theta\right) = \frac{-\boldsymbol{n} \cdot \nabla \rho}{|(\boldsymbol{t} \cdot \nabla \rho)\boldsymbol{t}|} = \frac{-\boldsymbol{n} \cdot \nabla \rho}{|\nabla \rho - (\boldsymbol{n} \cdot \nabla \rho)\boldsymbol{n}|}, \tag{22}$$

$$\boldsymbol{n} \cdot \nabla \rho = -\tan\left(\frac{\pi}{2} - \theta\right)|(\boldsymbol{t} \cdot \nabla \rho)\boldsymbol{t}|. \tag{23}$$

The discrete form of Eq. (22) can be expressed as

$$\rho_{i,j,1} = \rho_{i,j,2} + \tan\left(\frac{\pi}{2} - \theta\right)\zeta, \tag{24}$$

where the i and j indices denote the two orthogonal directions on the wall plane and the third index indicates the direction normal to the wall plane. Along the three-dimensional plane, the quantity $\zeta = |(\boldsymbol{t} \cdot \nabla \rho)\boldsymbol{t}|$ is expressed as

$$\zeta = \sqrt{(\rho_{i+1,j,2} - \rho_{i-1,j,2})^2 + (\rho_{i,j+1,2} - \rho_{i,j-1,2})^2}. \tag{25}$$

From the above form, we can achieve a desired wettability between the solid and the fluid by specifying the desired contact angle in Eq. (24). Once the density on the boundary points is specified, the normal gradient condition in Eq. (23) is satisfied in the solver. It is worth noting that we consider a constant contact angle mode in the present paper. The current model does not account for the large range of length scales associated with the moving contact lines. An alternative

modeling approach can be considered based on dynamic contact angle models [36,37], which however is not the focus of the current study.
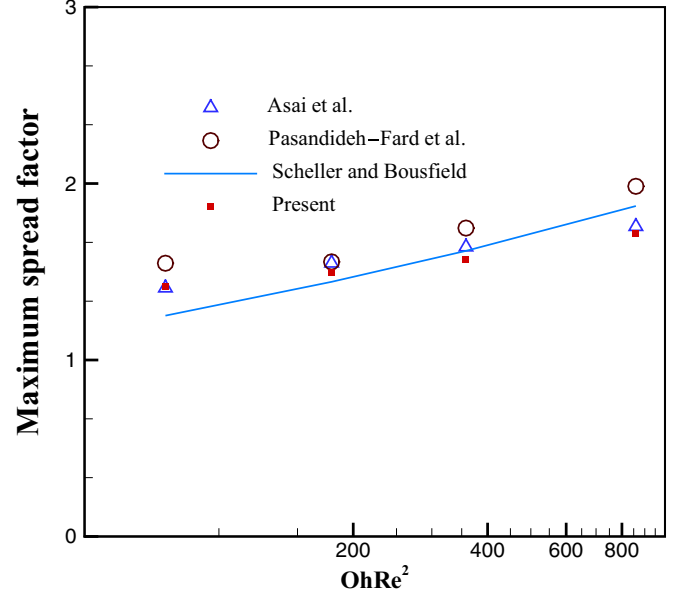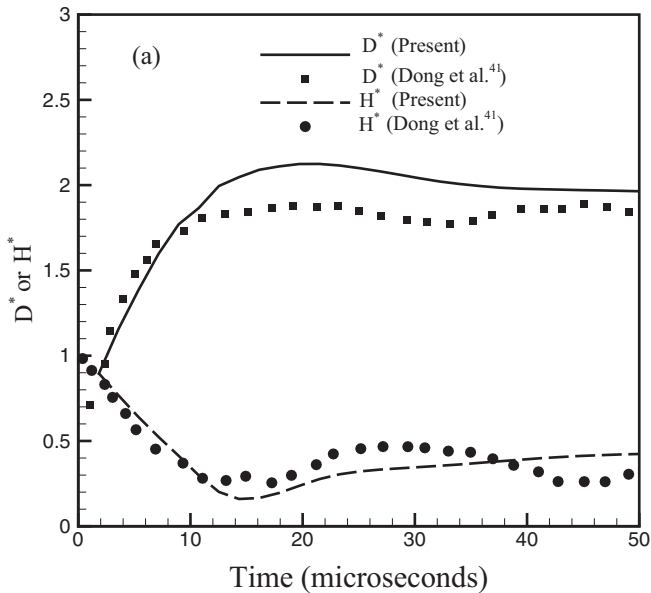
FIG. 3. Comparison of maximum spread factor from the present study with prediction equations for a single droplet impacting on a neutral wetting surface.

IV. NUMERICAL VALIDATION

Figure 3 shows the comparison of the maximum spread factor ($D^*_{\max}$), defined as the ratio of the maximum spread diameter with initial droplet diameter, for different values of Re and We with the well-known predictive trends [38–40]. A
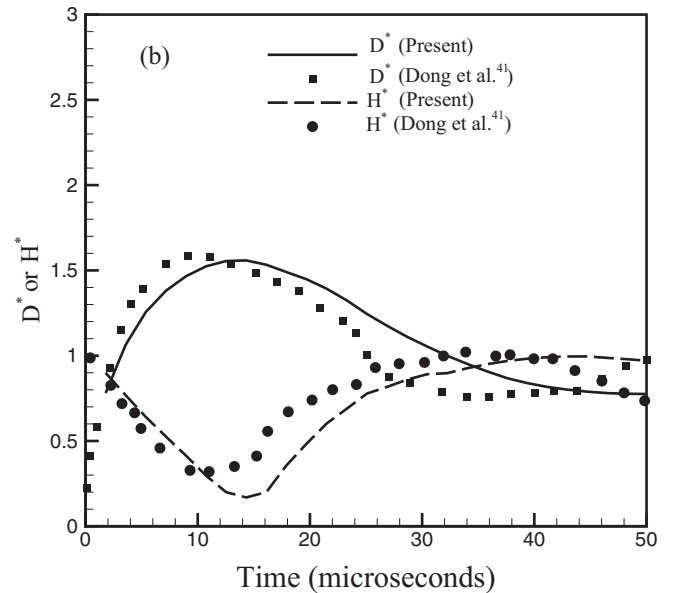
FIG. 4. Experimental validation of time evolution of spread factor D^* and droplet height H^* for We = 12.8 at the contact angles: (a) $\theta = 31°$ and (b) $\theta = 107°$.

TABLE I. Numerical convergence for the various droplet radii with Re = 600, We = 51.2, and $\theta = 140°$ at $T^* = 1.0$.

D_o (in lattice units)	50	70	84
D^*	1.599	1.666	1.694
Relative error	5.6%	1.65%	

spherical drop with diameter and interface thickness of 50 and 5 lattice units, respectively, was initialized.

A good comparison between the present computation and the prediction equation from previous literature is observed. Experimental validation of the present solver is accomplished by direct comparison of the dimensionless diameter or spreading factor D^* and the dimensionless height H^* with the results of Dong *et al.* [41]. Figure 4 illustrates the comparison for two different surface wettabilities: (a) 31° and (b) 107° with the droplet impinging with the Reynolds number and Weber number of Re = 241 and We = 12.8, respectively. A good agreement with the experimental results particularly in the initial stages of the impact is observed. The difference in the values of D^* between the experimental and the simulation results towards the later stages may be attributed to the pinning of the contact line which occurs due to contact angle hysteresis.

V. RESULTS AND DISCUSSION

After we validate the numerical model, we proceed to investigate the impact dynamics of the impacting droplet on an oscillating solid surface. We perform a grid independence test by comparing the spread factor (D^*) for droplets impacting with the same initial impact velocities at $U_A = 0.05$ and $\bar{\omega} = 1.0$ at $T^* = 1.0$. Table I shows D^* for three different grid resolutions at $T^* = 1.0$. Only a slight variation in D^* is observed for various D_o's. Based on the grid independence test, the droplet diameter is set to be 70 lattice units for the

simulations preformed in this study hereafter. The simulation is initialized with the droplet placed just in contact with the wall such that the distance between the wall and the droplet center is $0.5D_o$. The velocity of the moving wall at this instant is shown in Fig. 5(a) at $T^* = 0$ for the respective wave forms.

A. Effect of wave form geometry

The combined effects due to the interactions between the moving surface and the impacting droplet determine the final impact outcome and nonlinear dynamical interactions of the droplet with the oscillating wall. As such, we begin our investigations by exploring the influence of the wave form geometry of the oscillating substrate on the impinging droplet. We consider three different natures of wall velocity profiles, namely, *sine*, *triangle*, and *square wave form* for the oscillating substrate. Figure 5(a) shows the velocity profiles for one cycle of oscillation with oscillation amplitude $U_A = 0.15$ and frequency $\bar{\omega} = 1.0$. The temporal evolution of the droplet contact width for different wave forms is illustrated in Fig. 5(b). The observations indicate that the droplet undergoes rebound when the substrate is excited with the *sinusoidal* and *triangle* wave forms. However, the suppression of droplet rebound is observed when the surface oscillation is actuated with the *square* wave form. It is to be noted that droplet lift-off time when the surface oscillates with the *sinusoidal* wave form is greater than that of the *triangle* wave form. As the surface is excited with different wave profiles, the momentum transferred to the impinging droplet differs. The magnitude of this transferred momentum, which depends on the work performed by the oscillating surface on the impacting droplet, is proportional to the area under the curves shown in Fig. 5(a).

Hence, the surface excited with the *square* wave forms results in maximum momentum transport to the droplet liquid. When a droplet impinges on a stationary surface and reaches its maximum spread, the surface energy converts back into the kinetic energy resulting in droplet rebound. However,
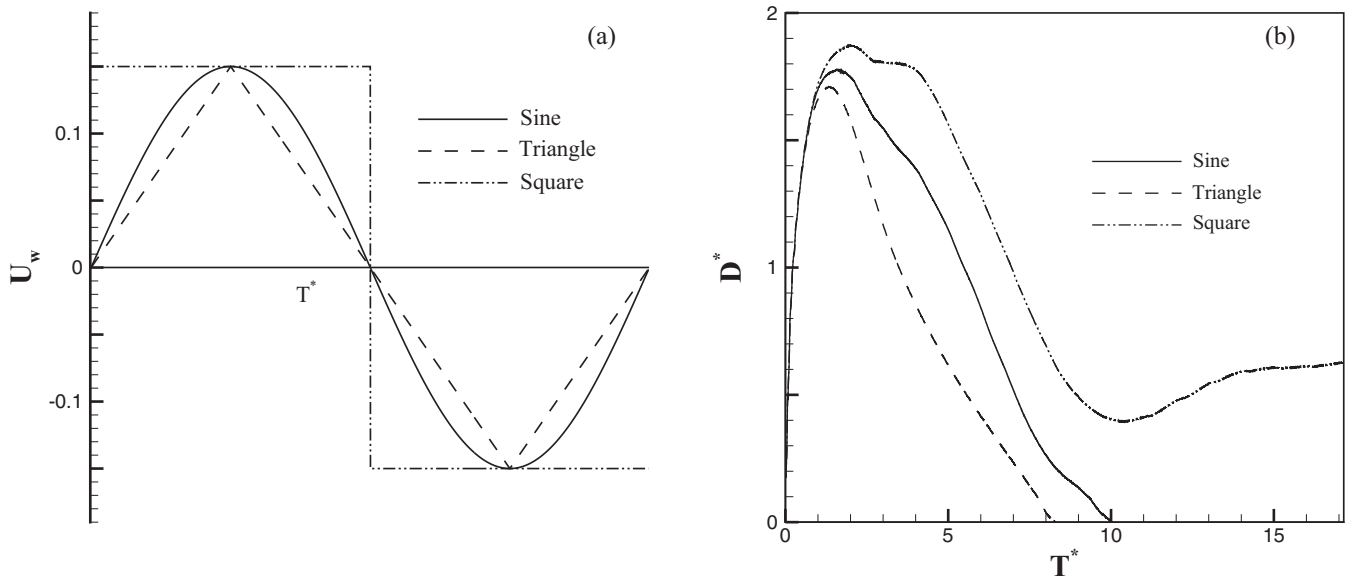
FIG. 5. (a) Profiles of the different wave forms for the oscillating substrate and (b) temporal evolution of the normalized contact width for different wave forms for velocity amplitude $U_A = 0.15$ and frequency $\bar{\omega} = 1.0$.
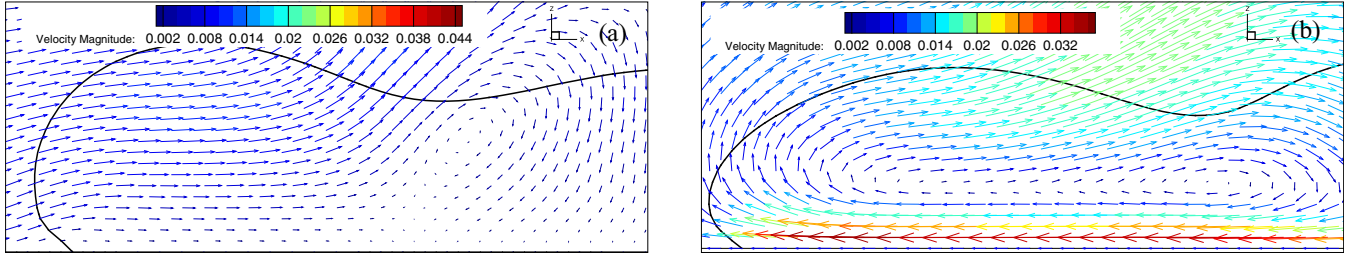
FIG. 6. Velocity field inside the droplet for two nonsinusoidal wave forms at $T^* = 2.0$ for $U_A = 0.15$ and $\bar{\omega} = 1.0$: (a) triangle and (b) square.

when the surface oscillates, the momentum transferred by the surface to the droplet liquid resists the surface tension forces as the droplet recoils. This leads to additional stretching of the droplet along the oscillating direction and prolongs droplet recoiling. Depending on the magnitude of momentum transferred, which in turn resists the surface tension forces, there can be different droplet impact outcomes. Figure 6 depicts the velocity flow field inside the droplet along the mid y plane for (a) *triangle* and (b) *square* wave forms at $T^* = 2.0$. The velocity field indicates the presence of high momentum fluid near the wall for case (b) unlike case (a) where the fluid near this region is almost stationary. A notable observation is the shape of the interface profiles observed for the two cases. The interface profile for the *square* wave form is stretched to a greater extent compared to the *triangle* wave form.

The interface profiles of the recoiling droplet for the three different wave forms are illustrated in Fig. 7 at $T^* = 4.0$. We observe capillary waves traveling along the droplet free surface for (a) *sinusoidal* and (c) *square* wave forms, whereas such characteristic waves are absent on the droplet surface with (b) the *triangle* wave form. Formation of such capillary waves has been observed on a droplet resting on a vibrating surface [42]. Different resonant modes of the droplet shapes can be observed by varying the vibration frequency. The droplet is more stretched with a narrow contact area for case (c) unlike case (a). The results presented in this section indicate that, out of the different wave forms tested, the *square* wave form promotes greater drop rebound suppression under a given set of impact conditions. Due to this desirable behavior, we explore the effect of different oscillation parameters on the drop impact outcome using the *square* wave form in the following subsections.

B. Effect of the oscillation phase at the instant of impact

What is the influence of the phase angle (ψ) of the oscillating wall at the instant of drop impingement on the impact outcome? Having fixed the geometry of the wave form of the oscillating wall, we next investigate the effect of the phase angle on the dynamics of the impacting droplet. We first consider the case with fixed oscillation frequency of $\bar{\omega} = 1.0$ for two different oscillation amplitudes. Figure 8 illustrates the temporal evolution of the contact diameter with (a) $U_A = 0.125$ and (b) $U_A = 0.15$ for different phase angles. In general, we observed that, for the given wave form and other impact conditions, the temporal evolution of the contact width is fairly independent of the phase angle as shown in Fig. 8. However, slight deviations in this behavior can be noticed around the region surrounding the maximum spread in both cases considered herein. This also is seen in the plot insets in (a) and (b). The *crashing time*, defined as the time taken by the droplet to undergo maximum spread, is around D_o/U_o, corresponding to $T^* = 1.0$. For the given $\bar{\omega}$ considered in this case, the wall completes the first half of its oscillation cycle at $T^* = 1.0$, corresponding to the *crashing time* when $\psi = 0$. As ψ increases, the time period between the instant of impact and the commencement of the second half of the cycle decreases. This implies that, for the considered cases with ψ greater than zero, the wall undergoes the second half of the oscillation cycle within the *crashing time*. From the numerical predictions illustrated from the inset plots, it can be inferred that the rate of increase in D^* is highest for $\psi = 0$ and lowest for $\psi = \pi/2$. We attribute this tendency to the duration in which unidirectional momentum is transferred from the moving wall to the inertia driven spreading droplet within its *crashing time*. An increase in this duration of unidirectional momentum transfer escalates droplet spreading along the
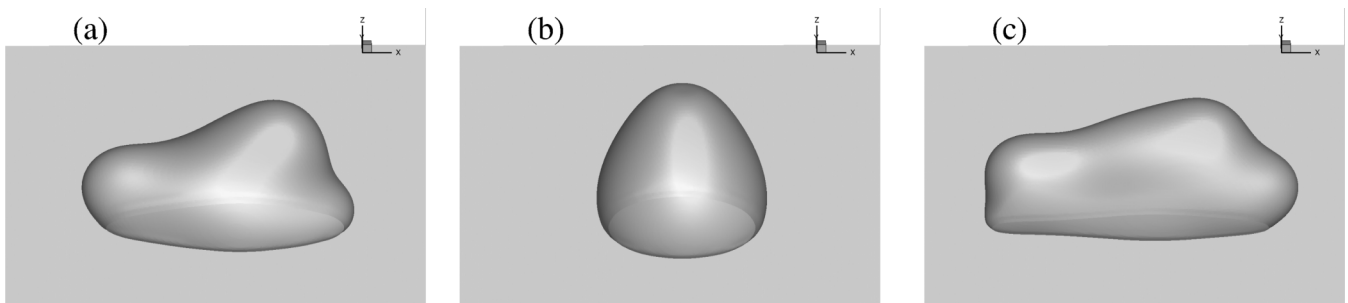
FIG. 7. Interface profiles of the impacting droplet for (a) sine, (b) triangle, and (c) square wave forms of the oscillating substrate with $U_A = 0.15$ and $\bar{\omega} = 1.0$ at $T^* = 4.0$.
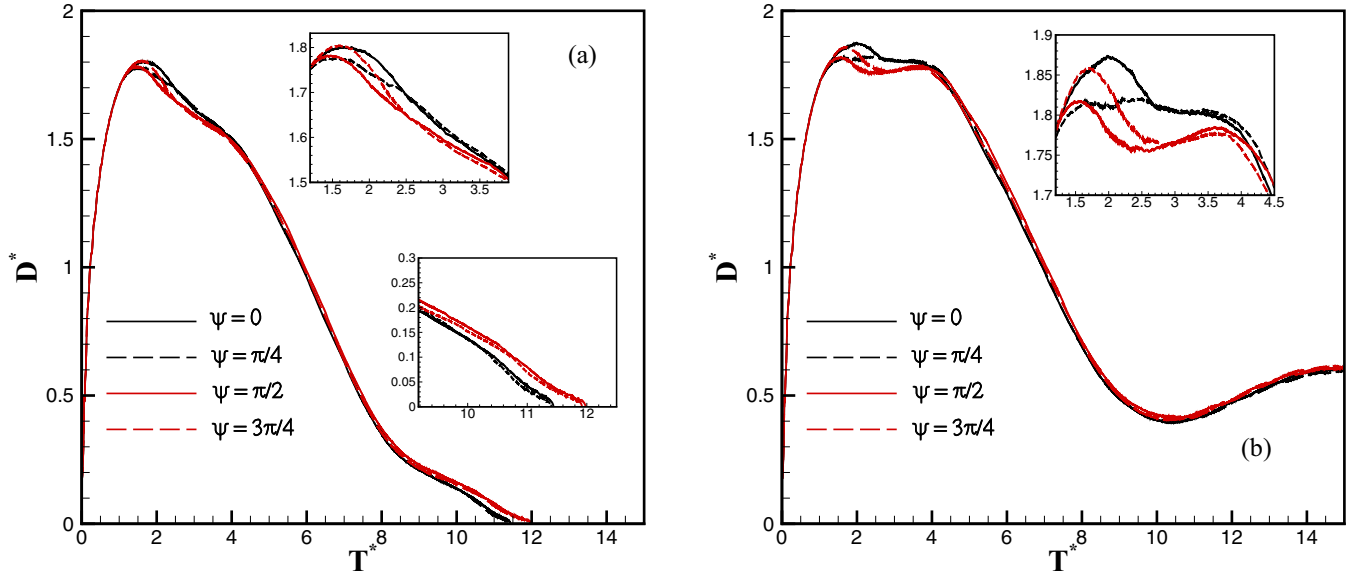
FIG. 8. Temporal evolution of the normalized contact width for different phase angles (ψ) at $\bar{\omega} = 1.0$ for two oscillation amplitudes: (a) $U_A = 0.125$ and (b) $U_A = 0.15$.

oscillating direction. The cases with $\psi = \pi/4$ and $3\pi/4$ have the same duration of unidirectional momentum transfer. As such we observe that, although evolution rate D^* for $\psi = 3\pi/4$ is initially higher than that with $\psi = \pi/4$, a reversal in this trend is noticed as time proceeds. This evolution trend in D^* around the region surrounding the maximum spread is amplified as U_A is increased.

We next investigate the cases wherein the oscillation amplitude is fixed at $U_A = 0.1$ while two different frequencies are considered. Figure 9 shows the temporal evolution of D^* for different phase angles with (a) $\bar{\omega} = 0.5$ and (b) $\bar{\omega} = 1.5$. For $\bar{\omega} = 0.5$ and $\psi = 0$, the commencement of the second half of the oscillation cycle begins at $T^* = 2.0$. Hence, for the

cases with $\psi = 0$ and $\pi/4$, there is a unidirectional momentum transfer from the wall to the impinging droplet even beyond its *crashing time* when it undergoes recoiling. We observe rebound suppression for both these cases with the evolution rate of D^* for $\psi = 0$ being higher than that with $\psi = \pi/4$ as shown in Fig. 9(a). This again can be attributed to the increase in the duration of unidirectional momentum transfer as discussed previously. For the remaining phase angles we observe droplet rebound. In either of these cases, the wall begins the second half of the oscillation cycle just after or within its *crashing time* corresponding to $\psi = \pi/2$ and $3\pi/4$, respectively. For the case with the increased frequency of $\bar{\omega} = 1.5$, we observe D^* being independent of ψ, leading to
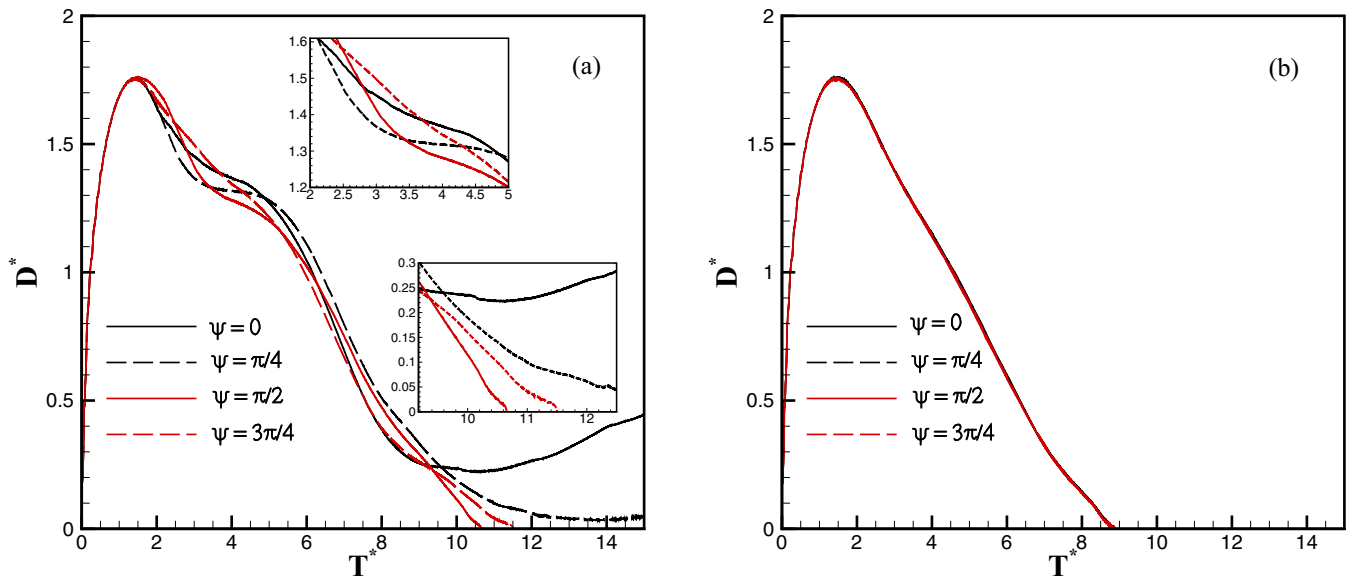
FIG. 9. Temporal evolution of the normalized contact width for different phase angles (ψ) with oscillation frequency (a) $\bar{\omega} = 0.5$ and (b) $\bar{\omega} = 1.5$ at $U_A = 0.1$.
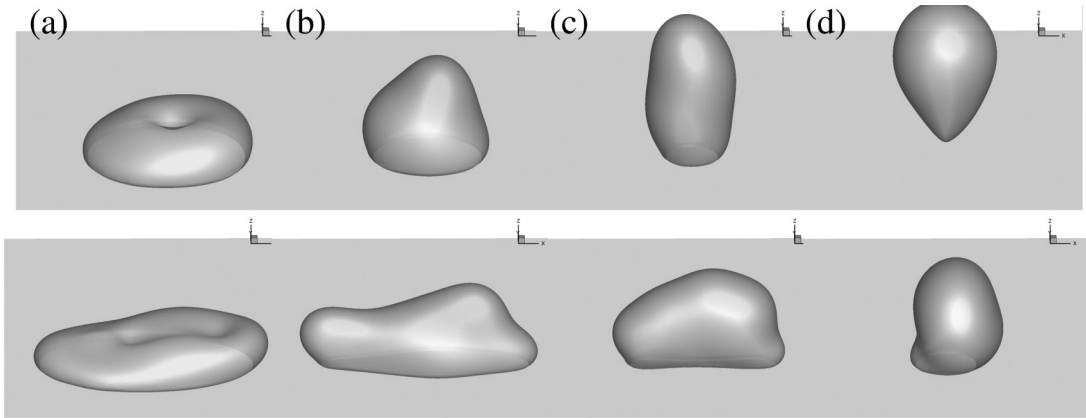
FIG. 10. Temporal evolution of impacting droplet (a) $T^* = 2.74$, (b) $T^* = 4.11$, (c) $T^* = 6.17$, and (d) $T^* = 8.91$ for $U_A = 0.05$ (top row) and $U_A = 0.15$ (bottom row) on a surface with $\bar{\omega} = 1.0$.

droplet rebound. We consider $\psi = 0$ for the remaining sections considered in this study.

C. Effect of oscillation amplitude and frequency

To investigate the effect of the amplitude of the oscillating substrate on the impact behavior, we fix the oscillation frequency $\bar{\omega}$ and the substrate contact angle to be 1 and 140°, respectively. Figure 10 displays the shape of the droplet at different time instants for $U_A = 0.05$ (top row) and 0.15 (bottom row).

The tangential momentum imparted by the moving substrate to the droplet liquid leads to greater elongation of the recoiling droplet along the direction of the wall oscillations. This elongation of the recoiling droplet increases with an increase in U_A as observed from the droplet shapes at $T^* = 2.74$. The droplet deformation is characterized by regions of varying local curvature along the drop surface. The magnitude of these local curvatures increases with an increase in U_A as observed from the droplet shapes at $T^* = 4.11$. The competing influence of the restoring effects of the Laplace pressure to minimize the surface area and the inertial forces inside the droplet supplemented by the momentum transferred by the moving substrate result in the generation of capillary waves

along the droplet surface. For $U_A = 0.05$, the droplet shape evolves into a columnlike structure ($T^* = 6.17$) and eventually lifts off the substrate. After it rebounds, the droplet evolves into a top-heavy mushroom shape as shown at $R^* = 8.91$. However, for $U_A = 0.15$, we notice that the droplet recoils and continues oscillating on the substrate. Hence, for the case with $U_A = 0.15$, the droplet rebound is suppressed.

We next investigate the effect of oscillation frequency ($\bar{\omega}$) of the moving surface on the morphology of the impacting droplet. The oscillation amplitude (U_A) is set to be 0.10 for the cases considered in this subsection. Figure 11 shows the time sequence of the impact process for $\bar{\omega} = 0.5$ (top row) and $\bar{\omega} = 1.5$ (bottom row). The time taken by the impacting droplet to spread to its maximum diameter τ_{max} is on the order of $(2R/U_o)$, whereas the time corresponding to the oscillation time period for $\bar{\omega} = 0.5$ is $4\tau_{max}$. This implies that the direction of momentum transfer between the wall and the droplet does not change during the inertial spreading phase as well as the early recoiling stage of the impact sequence. This results in asymmetric droplet spreading, leading to a greater accumulation of fluid inside the rim, which spreads along the direction of the wall motion. As the droplet attains its maximum spread diameter at the time τ_{max}, the surface tension forces begin to dominate, and the droplet begins to
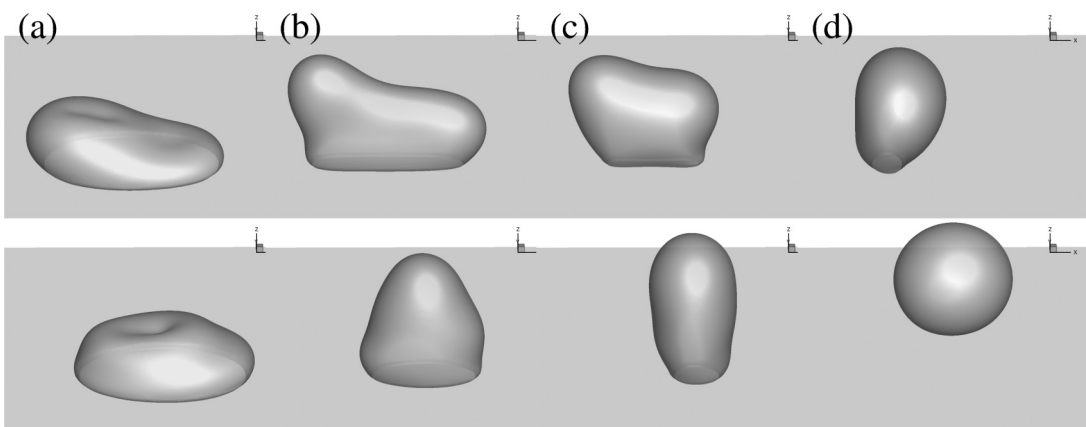
FIG. 11. Temporal evolution of impacting droplet at (a) $T^* = 3.08$, (b) $T^* = 5.14$, (c) $T^* = 6.85$, and (d) $T^* = 10.28$ for $\bar{\omega} = 0.5$ (top row) and $\bar{\omega} = 1.5$ (bottom row) on a surface with $U_A = 0.10$.

recoil. However, since the direction of the moving wall remains unchanged until $T^* = 2\tau_{\max}$, the asymmetry in the shape of the recoiling droplet is promoted with the fluid inside the droplet migrating from the downstream side towards the left rim. After time $T^* = 2\tau_{\max}$, there is a reversal in the direction of the wall motion. The direction of flow near the base of the droplet changes due to this reversal in the direction of the wall motion, leading to accumulation of the liquid inside the right rim. Owing to the inertia attained by the droplet liquid due to the initial wall movement, the direction fluid in the upper part of the droplet does not change during this cycle of wall motion. The height of the left rim increases as the droplet continues to recoil. This results in the formation of an asymmetric two lobed droplet morphology as observed at $T^* = 5.14$. The two lobes merge together under the influence of surface tension effects as the droplet completely recoils and oscillates on the surface. When $\bar{\omega}$ is increased to 1.5, we observe capillary waves traveling along the droplet surface due to the interactions between the surface tension forces and the momentum transferred by the oscillating substrate. Unlike the case with $\bar{\omega} = 0.5$, the droplet does not undergo large surface deformations along the direction of the oscillating wall and eventually rebounds off the surface.

Figures 12(a) and 12(b) illustrate the temporal evolution of the spread factor for different oscillation amplitudes and frequencies, respectively. After the initial increase in D^* due to inertial spreading, it is observed that D^* decreases as time progresses. For $U_A = 0.05$ and 0.10, the droplet rebound is observed as D^* approaches zero. It may be noted that the detachment time of the droplet increases with an increase in U_A. The evolution of the spread factor for $U_A = 0.15$ indicates rebound suppression as D^* increases after reaching its minimum spread around $T^* = 10.0$. Figure 12(b) illustrates the temporal evolution of the spread factor which reiterates the observations found from the time resolved images in Fig. 11. The evolution of D^* increases with the decrease in $\bar{\omega}$. As $\bar{\omega}$ increases, the time taken by the droplet to lift-off the substrate decreases.

To further characterize the behavior of the impacting droplet on oscillating substrates, we monitor the displacement of the X center of mass ($\Delta X_{\mathrm{c.m.}}$) of the droplet system from its initial position. The instantaneous X center of mass $X_{\mathrm{c.m.}}$ of the droplet is calculated by simple averaging over the entire domain enclosed by the interface,

$$X_{\mathrm{c.m.}} = \frac{\int_{V_{\mathrm{drop}}} x \, dV}{\int_{V_{\mathrm{drop}}} dV}, \tag{26}$$

where V_{drop} encloses the region of the density (ρ) greater than the mean density [$\rho^* = 0.5(\rho_l + \rho_g)$]. Figure 13 shows the time evolution of $\Delta X_{\mathrm{c.m.}}$ of the droplet for different values of oscillation amplitudes and frequencies. We notice that, in Fig. 13(a), there is a large shift in the position of the X center of mass of the droplet system during the first cycle of the wall oscillation. During the initial inertial spreading phase of the impact process, the droplet covers a larger contact area of the moving substrate. Hence, the tangential momentum transferred to the droplet liquid is higher resulting in a larger shift in the X center of mass of the droplet system during the initial cycles of the wall oscillations. As U_A increases, the tangential momentum transferred to the impacting droplet increases, leading to an increase in $\Delta X_{\mathrm{c.m.}}$. As time proceeds, the droplet begins to recoil, and the contact area decreases resulting in smaller fluctuations in $\Delta X_{\mathrm{c.m.}}$. A smooth and linear variation in $\Delta X_{\mathrm{c.m.}}$ is observed for $U_A = 0.05$ and 0.10 at later stages of impact due to the droplet rebound.

It is observed that at later times, for the case with $U_A = 0.15$, $\Delta X_{\mathrm{c.m.}}$ grows in magnitude as the droplet translates on the oscillating substrate. We may attribute such a shift in $\Delta X_{\mathrm{c.m.}}$ due to the combined interactions of the *swaying* motion of the oscillating free surface of the droplet and *spreading* of the droplet contact line. It is to be noted that the interactions between these two effects leading to the observed translation are triggered for a higher U_A. A recent study by Benilov and Billingham [43] demonstrated the interactions between the *swaying* and the *spreading* modes, which controlled the
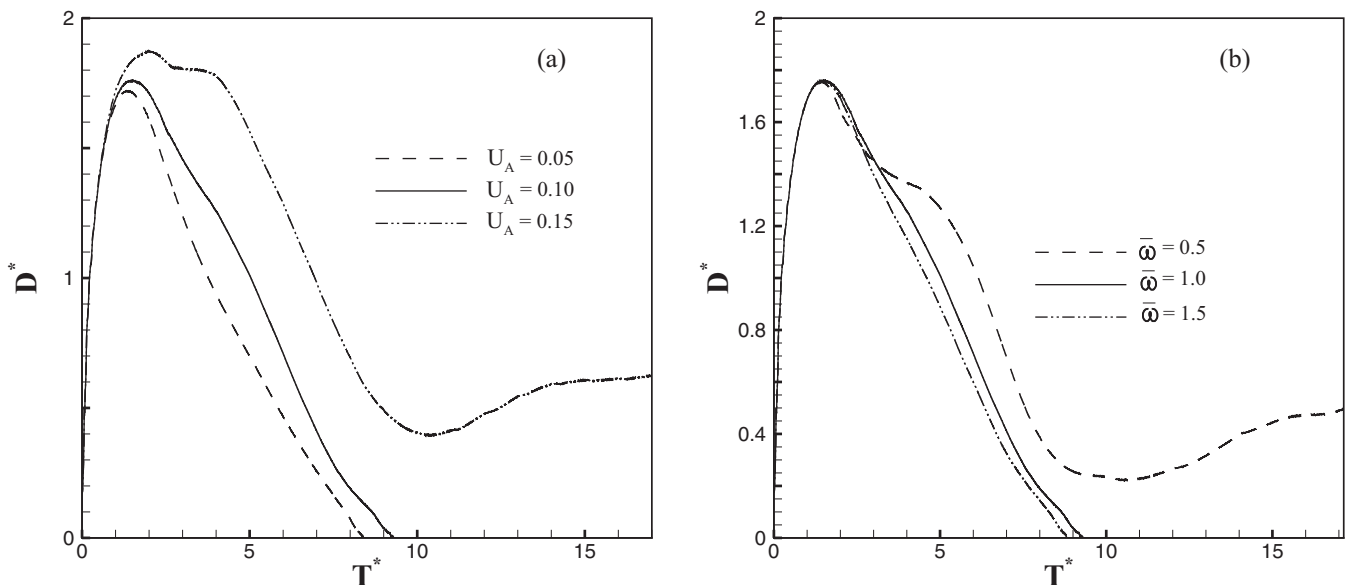
FIG. 12. Temporal evolution of the normalized contact width for different wall oscillation (a) amplitudes and (b) frequencies.
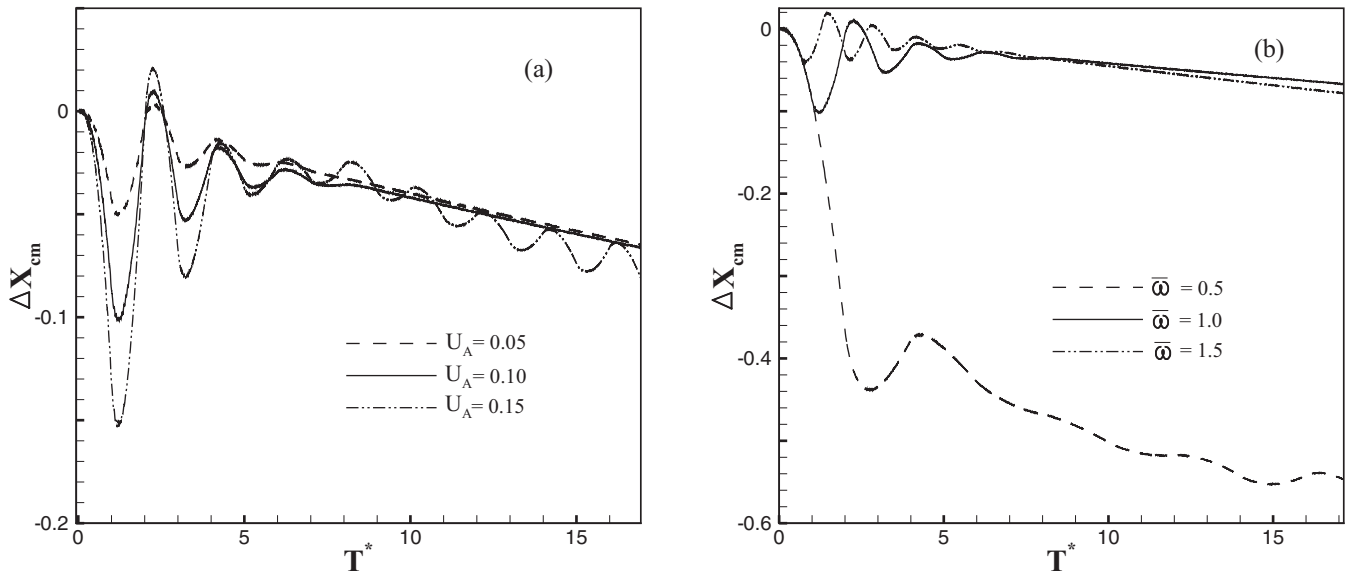
FIG. 13. Temporal evolution of the normalized shift in the X center of mass of the impacting droplet for different wall oscillation (a) amplitudes and (b) frequencies.

motion of liquid drops placed on an inclined plane oscillating vertically. They concluded that both modes were needed to make the drop climb uphill and the effect is strongest when they are in phase with each other. Whereas in their work [43], the direction in which the drop moves was determined by the specifics of the interaction between the two modes, in the present study the direction of shift is governed by the direction of the wall movement during the inertial spreading. The asymmetry introduced in the droplet shape during this period essentially determines the direction of this shift. Similar to the oscillatory nature of the mean velocity of the drop observed in Ref. [43], the temporal evolution of $\Delta X_{c.m.}$ for $U_A = 0.15$ exhibits an oscillatory nature in the present investigation.

The increased duration of unidirectional momentum transfer from the wall to the droplet in one direction for $\bar{\omega} = 0.5$ induces sufficient asymmetry in the droplet shape. This leads to a significant shift in the X center of mass of the droplet as seen from Fig. 13(b). As the wall reverses its direction and the liquid begins to accumulate in the right rim, a small rise in $\Delta X_{c.m.}$ is observed. At this stage of the impact process, the droplet is divided into two regions. A rising upper left region of the recoiling droplet comprising the large left rim and a region close to the wall including the smaller right rim. As the wall undergoes subsequent cycles of oscillations, the coupled interactions between the oscillating lower region and the surface tension driven recoiling upper region results in
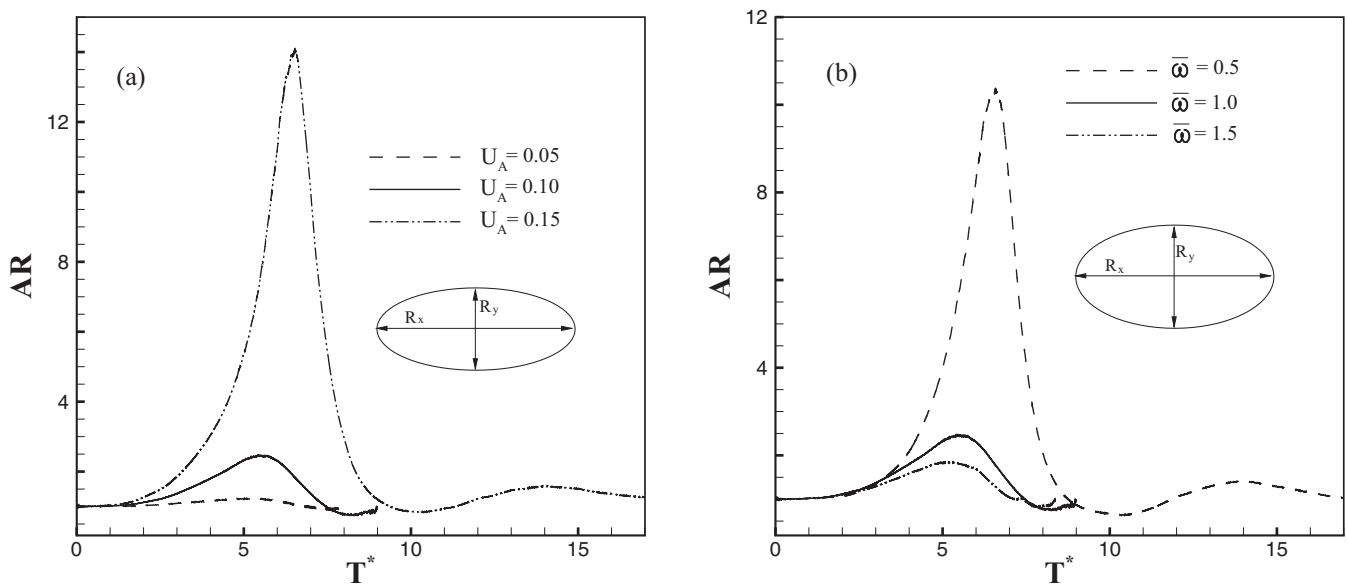
FIG. 14. Temporal evolution of the AR of the contact area for different wall oscillation (a) amplitudes and (b) frequencies.
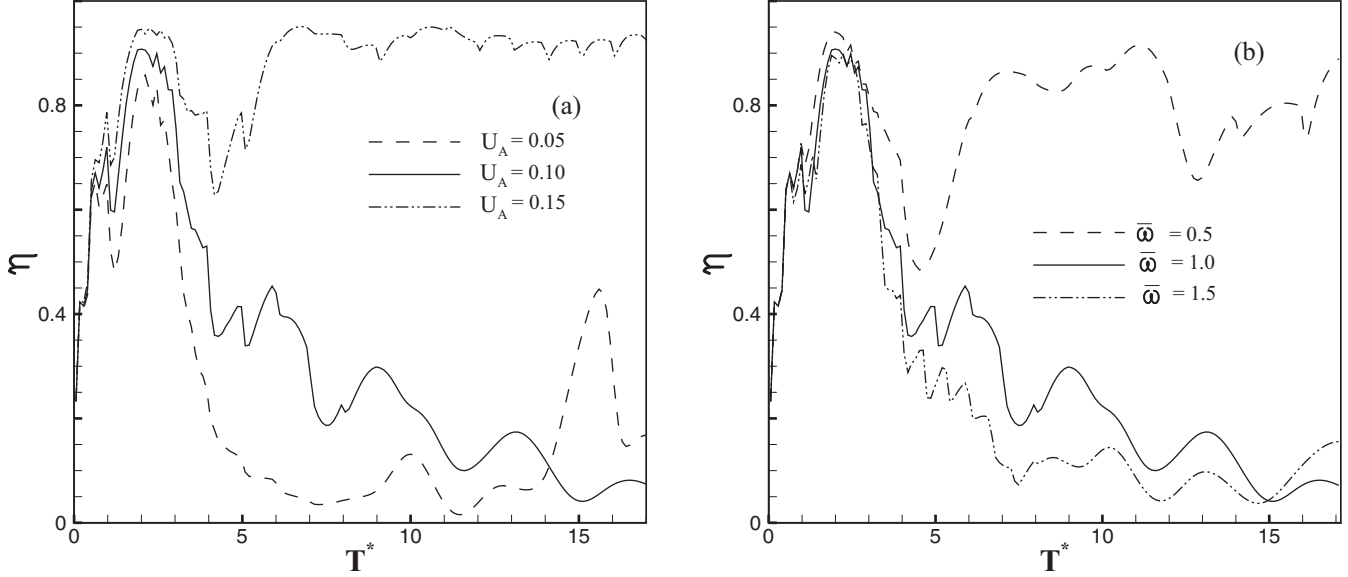
FIG. 15. Temporal evolution of the nonaxial distribution of the kinetic energy (η) for different wall oscillation (a) amplitudes and (b) frequencies.

a further shift in $\Delta X_{\text{c.m.}}$. This *lateral shifting* of the droplet from its initial location for the case with $\bar{\omega} = 0.5$ compared to the other two cases is attributed to the induced asymmetry in droplet shape due to the unidirectional transfer of momentum from the wall during the inertial spreading and the early retraction phase of the impact process.

Figure 14 illustrates the temporal evolution of the aspect ratio of the contact area given by $\text{AR} = (R_x/R_y)$. For $U_A = 0.05$, we observe that AR nearly stays close to 1.0 during its impact process until it lifts off the surface. The aspect ratio close to 1.0 implies that the contact line is circular in shape and it retracts with the peripheral forces along the contact line nearly acting uniformly towards its center. With an increase in U_A, we observe an increase in the evolution AR, which indicates slender and more elongated contact line shapes. Such shapes break the symmetry in the retraction process in comparison to a circular contact line. For $U_A = 0.15$, a sharp increment in the maximum value of the AR is observed. Unlike the other two cases considered, we observe a gradual rise in the AR after the droplet undergoes retraction. However, a decreasing trend in the evolution of the AR is noted for increasing oscillation frequencies as observed in Fig. 14(b). This is attributed to the unidirectional deformation of the contact line for lower $\bar{\omega}$ leading to elongated and slender shaped contact areas.

When a drop impacts on a solid surface, the initial kinetic energy of the droplet is converted into the surface energy of the spreading droplet, and a part of it dissipates due to viscous resistance. After reaching its maximum spread, the droplet undergoes recoiling during which the surface energy is converted back into the kinetic energy. When the surface is stationary, the kinetic energy is transferred primarily along the symmetry axis (Z axis), leading to droplet rebound. The presence of wall oscillations breaks down this symmetry in the distribution of the kinetic energy. The momentum transferred by the substrate leads to greater droplet deformation along the direction of the wall oscillations. This leads to greater

distribution of the kinetic energy along the principal X axis compared to the symmetric Z axis.

Figure 15 shows the nonaxial distribution of the kinetic energy (η) [44] defined as the ratio of the nonaxial kinetic energy to the total KE for different oscillation amplitudes,

$$\eta = \frac{\int_{V\,\text{drop}}(1/2)\rho\left(u_x^2 + u_y^2\right)dV}{\int_{V\,\text{drop}}(1/2)\rho\left(u_x^2 + u_y^2 + u_z^2\right)dV}, \qquad (27)$$

where u_x, u_y, and u_z are the x, y, and z components, respectively, of the velocity. Owing to the diffuse nature of the interface, oscillations are observed in the temporal distribution of η during the initial stages of impact. Therefore, to filter these oscillations, we plot the average values of η taken in an interval of every 200 time steps. It is apparent from Fig. 15(a) that the break down in the symmetric distribution of kinetic energy depends on the oscillation amplitude. When a droplet rebounds off the substrate, we notice a gradual decrease in η with time. However, for $U_A = 0.15$, we observe most of the kinetic energy of the droplet system distributed along the planar axes. Similarly, we observe significant transfer of the droplet kinetic energy across the planar axes after $T^* = 5.0$ for the case with $\bar{\omega} = 0.5$ in Fig. 15(b), during which the droplet undergoes *lateral shifting*. This reduces the kinetic energy transferred along the symmetric z axis and prevents droplet rebound unlike the other two cases considered.

A series of computations for different oscillation amplitudes and frequencies has been performed to construct a phase diagram of the amplitude versus frequency as shown in Fig 16(a). The phase diagram presents two regimes, namely, droplet *rebound* and *suppression* for $\text{Re} = 600$ and $\text{We} = 51.2$. It is observed that, although high values of frequency $\bar{\omega}$ and low amplitude U_A favor the occurrence of droplet *rebound*, the converse is true for droplet *deposition*. As discussed previously, this behavior is attributed to the transfer of the initial kinetic energy along the planar axes for higher U_A and
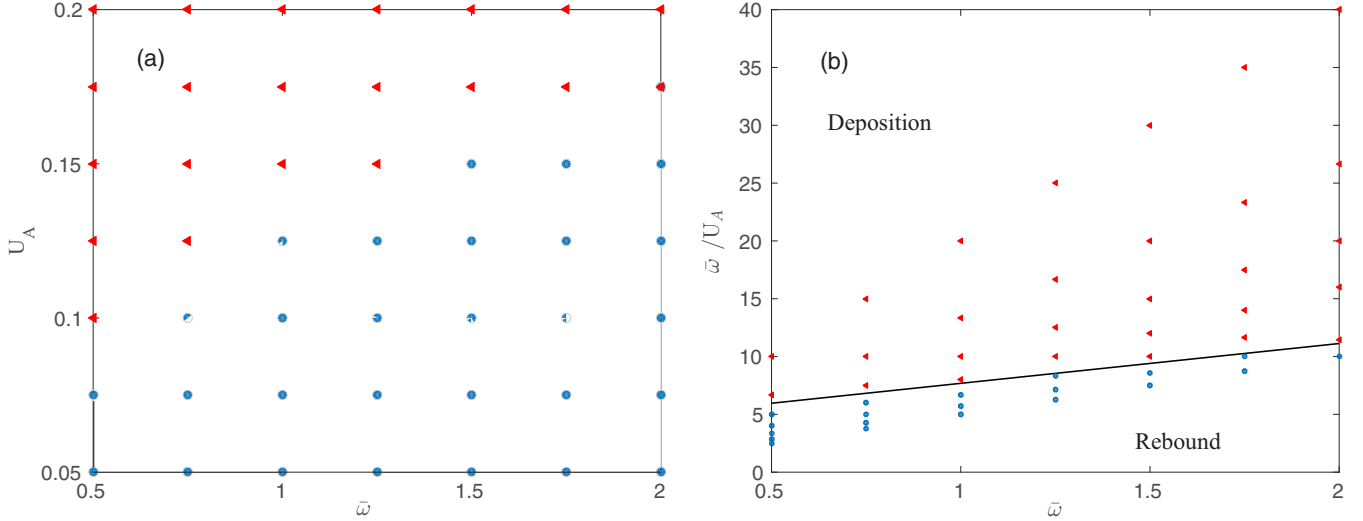
FIG. 16. Phase diagram for droplet rebound suppression: (a) oscillation amplitude versus frequency $\bar{\omega} - U_A$, (b) scaled diagram $\bar{\omega}$-$(\bar{\omega}/U_A)$ for the droplet rebound and deposition regimes. The $\circ$ and $\triangleleft$ symbols represent rebound and deposition regimes, respectively.

lower $\bar{\omega}$ leading to droplet *deposition*. Hence, an optimum choice of $\bar{\omega}$ and U_A can result in different outcomes of the impact process. It can be observed from the regime map as shown in Fig. 16(a) that a nearly linear trend close to the transition region between the two regimes exists. To further elucidate this trend along the transition region, we scale $\bar{\omega}$ with the oscillation amplitude U_A and plot a different scaled flow regime map ($\bar{\omega}$ versus $\bar{\omega}/U_A$) as shown in Fig. 16(b). This leads to the rescaling of the frequency using the oscillating speed instead of on the initial impact speed of the impinging droplet. The figure clearly illustrates the linear trend along the transition region. A best fit curve is plotted in the regime map separating the *rebound* and *deposition* modes, which is given by the following linear relationship:

$$\bar{\omega}/U_A = M\bar{\omega} + C, \qquad (28)$$

where the slope coefficient is $M = 3$ and the intercept is $C = 4.2$.

VI. KINEMATICS AND ENERGETICS OF REBOUND SUPPRESSION

In order to elucidate the essential mechanism of rebound suppression of a droplet subjected to wall oscillation, we compare the instantaneous velocity field inside the droplet along the symmetry plane between a nonoscillating and an oscillating surface. Figure 17 illustrates these flow fields inside the drop with the left and the right columns corresponding to the nonoscillating and the oscillating cases, respectively. The oscillation amplitude and frequency for the case considered in this section are set to be 0.15 and 1.0, respectively. In general, the process of normal drop impact on a stationary solid surface can be classified into three stages: *symmetric inertial spreading*, *recoiling*, and attainment of *equilibrium configuration*. The presence of an oscillating surface translates the *symmetric inertial spreading* stage into *asymmetric inertial spreading*. This asymmetric behavior is attributed to the accumulation of the droplet liquid inside the inertia driven

spreading rim moving in phase with the oscillating wall. Once the drop attains its maximum spread, the role of the wall oscillation becomes significant in determining the impact outcome. When the droplet begins to recoil for the nonoscillating case, the liquid inside the peripheral rims is directed upward towards the central axis of symmetry. This behavior is illustrated from the velocity field inside the drop as shown in Fig. 17(a) at $T^* = 4.104$ and 5.814. This stage constitutes the *recoiling* phase of the impact process. We notice that during this phase the magnitude of velocity field near the base of the droplet is relatively low compared to the motion of the bulk fluid in the upper region, which leads to its vertical elongation. The drop continues to elongate and detaches from the surface resulting in rebound. As the drop is airborne, we observed intense recoiling of the trailing end of the drop, which is depicted from the velocity field in this region as shown at $T^* = 8.892$. The presence of wall oscillations along the direction normal to the impact line breaks the uprising central symmetry of the flow field during the *recoiling* phase, which is observed for the nonoscillating situation. The high momentum fluid in contact with the oscillating wall, resulting due to the no-slip condition, is observed from the velocity field shown in Fig. 17(b) and transfers this momentum to the adjoining bulk droplet fluid. This leads to the movement of the droplet liquid transversely along the oscillating direction and restricts its bulk uprising, thereby breaking the uprising central symmetry of Fig. 17(a). The velocity field inside the bulk region of the drop at $T^* = 5.814$ is in line with this observation. Due to this transverse movement of the bulk fluid and under the influence of the restoring effects of surface tension forces, the receding phase is characterized by the generation of waves along the droplet surface. Hence, we assign this stage of the impact process as *recoiling with surface waves*. It can be concluded that the primary cause of rebound suppression is related to the interference of the sideways motion in the droplet interior. This in turn breaks the uprising symmetry in the velocity distribution as observed for the nonoscillating case. Finally, as the drop recoils and attains a spherical configuration,
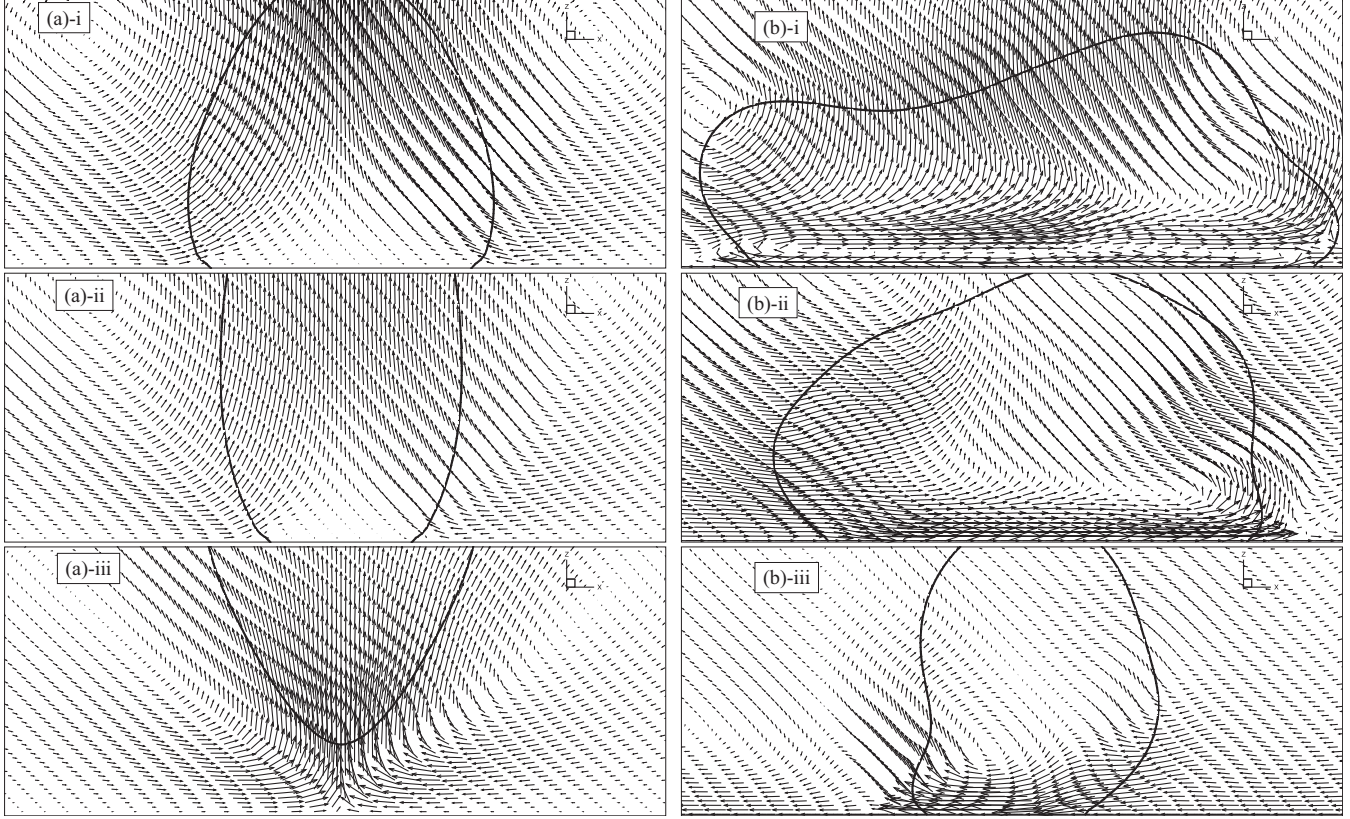
FIG. 17. Instantaneous velocity field inside the droplet along the symmetry plane at (i) $T^* = 4.104$, (ii) $T^* = 5.814$, and (iii) $T^* = 8.892$ for (a) the nonoscillating and (b) the oscillating cases with $U_A = 0.15$ and $\bar{\omega} = 1.0$.

we observe that only the region close to the wall is driven by the high momentum fluid in contrast to its bulk. This leads to the final *oscillatory equilibrium* phase of the impact process.

To further quantify the above discussed mechanism for rebound suppression, we monitor the axial kinetic energy coefficients given as follows:

$$\eta_i = \frac{\left[\int_{V\,\mathrm{drop}}(1/2)\rho\left(u_i^2\right)dV\right]_{\mathrm{oscillating}}}{\left[\int_{V\,\mathrm{drop}}(1/2)\rho\left(u_i^2\right)dV\right]_{\mathrm{nonoscillating}}}, \qquad (29)$$

where i corresponds to the principal coordinate axis along the X, Y, and Z directions. Figure 18 illustrates the temporal evolution of η_i along the three directions. The observations clearly indicate that the major portion of the kinetic energy is transferred along the X axis, followed by the Y and Z axes. As time proceeds, we notice a sharp rise in η_x and η_y between $T^* = 6$ and 9. During this period the drop undergoes vigorous recoiling. A part of this excess kinetic energy is converted into surface waves traveling its surface, whereas some part the kinetic energy is dissipated due to the viscous effects. This can be attributed from the temporal evolution surface energy (E_{se}) as shown in Fig. 19. The surface energy is obtained from the free-energy density model employed in our simulations,

$$E_S^* = \int_V (E_o + \kappa|\boldsymbol{\nabla}\rho|^2)dV, \qquad (30)$$

where $E_o = \beta(\rho - \rho_v^{\mathrm{sat}})^2(\rho - \rho_l^{\mathrm{sat}})^2$. The figure clearly illustrates the increase in surface energy of the droplet impinging

on an oscillating surface in comparison with a nonoscillating surface. The droplet impacting on the nonoscillating case continues its vertical elongation and eventually rebounds off the surface. This implies that most of the kinetic energy for this case is transferred along the Z axis instead of the other two principal axes. The temporal evolution of η_z clearly indicates
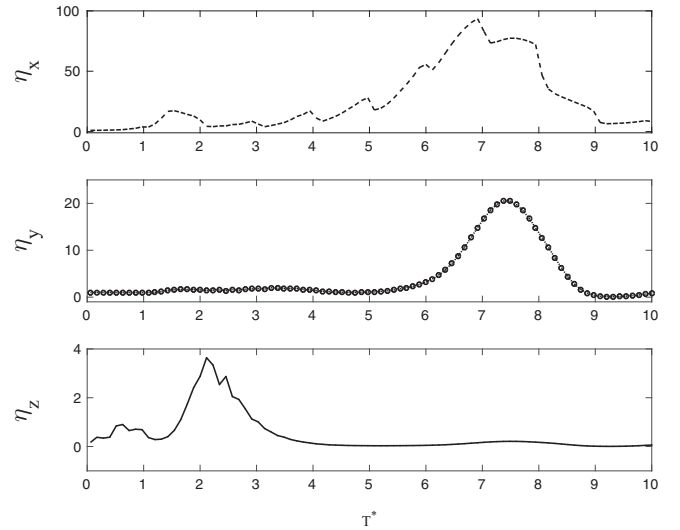
FIG. 18. Temporal evolution of the ratio of kinetic energy of the droplet along the principal axes between oscillating and nonoscillating walls.
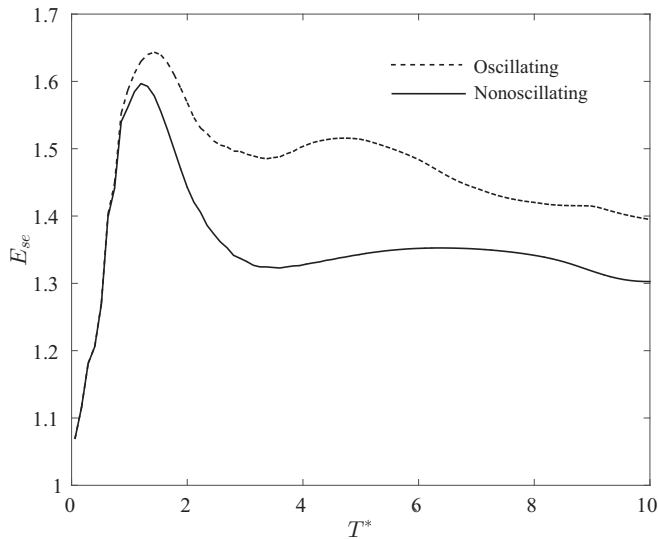
FIG. 19. Temporal evolution of the surface energy of the impinging drops on oscillating and nonoscillating surfaces. The energy is nondimensionalized by σR_o^2.

the suppression of kinetic energy transfer along the Z direction with η_Z being less than 1 for most of the impact duration.

VII. CONCLUSIONS

We have performed a three-dimensional numerical investigation on the impact dynamics of a droplet on an oscillating solid surface. A high-density ratio based phase field lattice Boltzmann method was employed in conjunction with a geometric based contact line formulation for the moving contact line. This paper proposed a method to suppress the drop rebound by substrate oscillation normal to the impact direction. The wave nature of the oscillating surface was observed to play a significant role on the impact behavior and rebound suppression. Of the various tested wave forms in the current study, we observed that the *square* wave form promotes a greater amount of drop rebound suppression. It is found that, for cases with low oscillation frequencies, the phase of the oscillation wall influenced the impact outcome. A systematic numerical study demonstrated the dominant effect of oscillation amplitude and frequency for mitigating droplet rebound. Droplet rebound suppression was found to be generally favored by high oscillation amplitudes and low frequencies. For a given range of oscillation amplitude and frequency, a phase diagram has been constructed which summarizes the impact outcome in the form of droplet rebound and deposition regimes. Reconstructing the phase diagram with a scaled oscillation amplitude clearly indicates a linear trend in the transition region between the two regimes. Low frequency oscillations coupled with high amplitudes resulted in the lateral shifting of the droplet from its impact position. The interplay of the inertial time scale and the oscillation time period played a major role in lateral shifting of droplet impacting on the solid wall. Although the current simulation results present a method for drop rebound suppression, the flow regimes described in this paper need to be confirmed by experiments. The effect of gravity has been neglected in this study, which will induce additional dynamics for large impinging droplets. Thus further research remains to be explored on this topic of droplet rebound suppression.

[1] A. L. Yarin, Drop impact dynamics: Splashing, spreading, receding, bouncing, Annu. Rev. Fluid Mech. **38**, 159 (2006).

[2] M. Rein, Phenomena of liquid drop impact on solid and liquid surfaces, Fluid Dyn. Res. **12**, 61 (1993).

[3] R. Rioboo, C. Tropea, and M. Marengo, Outcomes from a drop impact on solid surfaces, Atomization Sprays **11**, 155 (2001).

[4] K. M. Wisdom, J. A. Watson, X. Qu, F. Liu, G. S. Watson, and C. H. Chen, Self-cleaning of super-hydrophobic surfaces by self-propelled jumping condensate, Proc. Natl. Acad. Sci. U.S.A. **110**, 7992 (2013).

[5] J. B. Boreyko and C. H. Chen, Self-Propelled Dropwise Condensate on Super-Hydrophobic Surfaces, Phys. Rev. Lett. **103**, 184501 (2009).

[6] K. Rykaczewski, A. T. Paxon, S. Anand, X. Chen, Z. Wang, and K. K. Varanasi, Multimode multidrop serial coalescence effects during condensation on hierarchical super-hydrophobic surfaces, Langmuir **29**, 881 (2013).

[7] R. D. Narhe, W. González-Vinas, and D. A. Beysens, Water condensation on zinc surfaces treated by chemical bath deposition, Appl. Surf. Sci. **256**, 4930 (2010).

[8] W. M. Grissom and F. A. Wierum, Liquid spray cooling of a heated surface, Int. J. Heat Mass Transf. **24**, 261 (1981).

[9] D. Soltman and V. Subramanian, Inkjet-printed line morphologies and temperature control of the coffee ring effect, Langmuir **24**, 2224 (2008).

[10] S. D. Aziz and S. Chandra, Impact, recoil and splashing of molten metal droplets, Int. J. Heat Mass Transf. **43**, 2841 (2000).

[11] W. Wirth, S. Storp, and W. Jacobsen, Mechanisms controlling leaf retention of agricultural spray solutions, Pestic. Sci. **33**, 411 (1991).

[12] V. Bergeon, D. Bonn, J. Y. Martin, and L. Vovelle, Controlling droplet deposition with polymer additives, Nature (London) **45**, 772 (2000).

[13] M. Aytouna, D. Bartolo, G. Wegdam, D. Bonn, and S. Rafai, Impact dynamics of surfactant laden drops: Dynamic surface tension effects, Exp. Fluids **48**, 49 (2010).

[14] W. Deng and A. Gomez, The role of electric charge in microdroplets impacting on conducting surfaces, Phys. Fluids **22**, 051703 (2010).

[15] S. Mangili, C. Antonini, M. Marengoa, and A. Amirfazli, Understanding the drop impact phenomenon on soft pdms substrates, Soft Matter **8**, 10045 (2012).

[16] C. Antonini, F. Villa, I. Bernagozzi, A. Amirfazli, and M. Marengo, Drop rebound after impact: The role of the receding contact angle, Langmuir **29**, 16045 (2013).

[17] K. A. Raman, R. K. Jaiman, T. S. Lee, and H. T. Low, Lattice boltzmann simulations of droplet impact onto surfaces with varying wettabilities, Int. J. Heat Mass Transf. **95**, 336 (2016).

[18] P. K. Unnikrishnan, V. Vaikuntanathan, and D. Sivakumar, Impact dynamics of high weber number drops on chemically modified metallic surfaces, Colloids Surf., A **459**, 109 (2014).

[19] S. Yun, J. Hong, and K. H. Kang, Suppressing drop rebound by electrically driven shape distortion, Phys. Rev. E **87**, 033010 (2013).

[20] H. J. Lee and H. Y. Kim, Control of drop rebound with solid target motion, Phys. Fluids **16**, 10 (2004).

[21] Li-Shi Luo, Theory of the lattice Boltzmann method: Lattice Boltzmann models for nonideal gases, Phys. Rev. E **62**, 4982 (2000).

[22] S. Chen and G. Doolen, Lattice boltzmann method for fluid flows, Annu. Rev. Fluid Mech. **30**, 329 (1998).

[23] K. Sun, M. Jia, and T. Wang, Numerical investigation of head-on droplet collision with lattice boltzmann method, Int. J. Heat Mass Transf. **58**, 260 (2013).

[24] S. Zhao, A. Riaud, G. Luo, Y. Jin, and Y. Cheng, Simulation of liquid mixing inside micro-droplets by a lattice boltzmann method, Chem. Eng. Sci. **28**, 118 (2015).

[25] A. K. Gunstensen, D. H. Rothman, S. Zaleski, and G. Zanetti, Lattice boltzmann model of immiscible fluids, Phys. Rev. A **43**, 4320 (1991).

[26] D. H. Rothman and J. M. Keller, Immiscible cellular-automaton fluids, J. Stat. Phys. **52**, 1119 (1988).

[27] X. Shan and H. Chen, Lattice boltzmann for simulating flows with multiple phases and components, Phys. Rev. E **47**, 1815 (1993).

[28] M. R. Swift, W. R. Osborn, and J. M. Yeomans, Lattice boltzmann for simulations for liquid-gas and binary fluid systems, Phys. Rev. E **54**, 5041 (1996).

[29] X. He, X. Shan, and R. Zhang, A lattice boltzmann scheme for incompressible multiphase flow and its application insimulation of rayleigh taylor instability, J. Comput. Phys. **152**, 642 (1999).

[30] T. Lee and C. L. Lin, A stable discretization of the lattice boltzmann equation for simulation of incompressible two-phase flows at high density ratio, J. Comput. Phys. **206**, 16 (2005).

[31] D. Jamet, O. Lebaigue, N. Coutris, and J. M. Delhaye, The second gradient method for the direct numerical simulation of liquid vapor flows with phase change, J. Comput. Phys. **169**, 624 (2001).

[32] P. Lallemand and L. S. Luo, Lattice boltzmann method for moving boundaries, J. Comput. Phys. **184**, 406 (2003).

[33] K. A. Raman, R. K. Jaiman, T. S. Lee, and H. T. Low, Lattice boltzmann study on the dynamics of successive droplets impact on a solid surface, Chem. Eng. Sci. **145**, 181 (2016).

[34] H. Ding and P. D. M. Spelt, Wetting condition in diffuse interface simulations of contact line motion, Phys. Rev. E **75**, 046708 (2007).

[35] L. Wang, H. Huang, and X. Y. Lu, Scheme for contact angle and its hysteresis in a multiphase lattice boltzmann method, Phys. Rev. E **87**, 013301 (2013).

[36] E. B. Dussan, V, On the spreading of liquids on solid surfaces: Static and dynamic contact lines, Annu. Rev. Fluid Mech. **11**, 371 (1979).

[37] Y. Sui, H. Ding, and P. D. M. Spelt, Numerical simulations of flows with moving contact lines, Annu. Rev. Fluid Mech. **46**, 97 (2014).

[38] A. Asai, M. Shioya, S. Hirasawa, and T. Okazaki, Impact of an ink drop on paper, J. Imaging Sci. Technol. **37**, 205 (1993).

[39] M. Pasandideh-Fard, Y. M. Qiao, S. Chandra, and J. Mostaghimi, Capillary effects during droplet impact on a solid surface, Phys. Fluids **8**, 650 (1996).

[40] B. L. Scheller and D. W. Bousfield, Newtonian drop impact with a solid surface, AIChE **41**, 1357 (1995).

[41] H. Dong, W. W. Carr, D. G. Bucknall, and J. F. Morris, Temporally-resolved inkjet drop impaction on surfaces, AIChE **53**, 2606 (2007).

[42] L. Dong, A. Chaudhury, and M. K. Chaudhury, Lateral vibration of a water drop and its motion on a vibrating surface, Eur. Phys. J. E **21**, 231 (2006).

[43] E. S. Benilov and J. Billingham, Drops climbing uphill on an oscillating substrate, J. Fluid Mech. **674**, 93 (2011).

[44] S. Yun and G. Lim, Ellipsoidal drop impact on a solid surface for rebound suppression, J. Fluid Mech. **752**, 266 (2014).